https://doi.org/10.1016/j.apsusc.2021.150252

Bi^{3+} occupancy rearrangement in $K_{2-x}A_xMgGeO_4$ phosphor to achieve ultra-broad-band white emission based on alkali metal substitution engineering

Haifeng Zhu[a,b,1], Shuqing Feng[a,b,1], Zihui Kong[a], Xu Huang[a], Lu Peng[a], Jing Wang[c,d], Wai-Yeung Wong[e], Zhi Zhou[a,b], Mao Xia[a,b]*

[a]School of Chemistry and Materials Science, Hunan Agricultural University, Changsha, 410128, P.R. China

[b]Hunan Optical Agriculture Engineering Technology Research Center, Changsha, 410128, P. R. China

[c]State Key Laboratory of Optoelectronic Materials and Technologies, School of Chemistry, Sun Yat-Sen University, Guangzhou 510275, PR China

[d]School of Materials Science and Engineering, Sun Yat-Sen University, Guangzhou 510275, PR China

[e]Department of Applied Biology and Chemical Technology, The Hong Kong Polytechnic University, Hung Hom, Hong Kong, PR China

***Corresponding authors:**

Prof. Mao Xia

Phone number: (+86)-15802612087; **E-mail:** xiamao2019@hunau.edu.cn

[1] Haifeng Zhu and Shuqing Feng contributed equally to this work.

Abstract:

Ultra-broad-band white emitting phosphors have a wide application prospect in the new generation of illumination systems. Due to the sensitivity of Bi^{3+} to the surrounding environment, it exhibits different luminescence properties in different crystallographic sites, which makes it easy to achieve white emission. Cationic substitution engineering is the most effective strategy for controlling the environment around Bi-site and realizing the spectrum tuning. Herein, we conducted substitution engineering in $K_2MgGeO_4:Bi^{3+}$ that uses alkali metal A^+ (A = Li, Na, Rb) to substituted K^+. The difference in emission spectrum excited at various wavelengths is related to extra luminescent centers generation and Bi^{3+} occupancy rearrangement in KMGO:Bi^{3+} under the influence of Li^+ and Na^+, which also leads to the expansion of full widths at half-maximum (FWHM) to 204 nm forming a bright white emission. Besides, the modulation of Rb^+ increases the activation energy and enhances its thermal stability to 88.66%. The high R_a values (93.4) of the fabricated WLED indicate that $K_{1.456}Na_{0.54}MgGeO_4:0.004Bi^{3+}$ could be used as a single-component white phosphor in solid-state lighting. Our research shows that alkali metal substitution engineering is of great significance to controlling the luminescence emission and improving the thermal stability of luminescent materials.

Keywords: $K_2MgGeO_4:Bi^{3+}$; Substitution engineering; Tunable emission; Ultra-broad-band white emission; WLED.

1. Introduction

Phosphor-converted white-light-emitting diodes (pc-WLEDs), with the advantages of high luminescence efficiency, excellent durability and low production costs, have innovated the entire lighting industry [1-3]. At present, white light emission of pc-LED is realized mainly through the following four ways: (i) blue chip + yellow phosphor; (ii) blue chip + green/red or green/yellow/red phosphors; (iii) UV or n-UV LED chip + blue/green/red or blue/green/yellow/red phosphors; (iv) UV or n-UV LED chip + broad band white phosphor [4-7]. Among them, the fourth way is considered to be the most optimal strategy to obtain white emission, since it has a lower correlated color temperature (CCT) and a more suitable color rendering index (R_a). More importantly, the phenomenon of reabsorption between multiphase phosphors and the problem of color aberrations at high temperatures could be effectively avoided in this method [8-10]. Hence, it's a hot research project to design and obtain single-phase white phosphors with broad FWHM.

As far as the commonly used pc-WLEDs phosphors are concerned, the number of white emitting compounds is quite restricted. Nowadays, plentiful research on white phosphors are mainly concentrated on the rare-earth ions (Eu^{2+}, Ce^{3+}) such as $Sr_2AlSi_2O_6N:Eu^{2+}$ [8], $Sr_3Ce(PO_4)_3:Eu^{2+}$ [11], $Sr_3Sc_4O_9:Ce^{3+}$ [12], $Y_3Si_5N_9O:Ce^{3+}$ [13] etc. However, the unbalanced white light emission caused by the partial overlap of excitation and emission bands makes their emission bands far away from the light sensitive area of human eye (400-700 nm), which limits the application of these types of phosphor in pc-LED industry [14, 15]. Based on this situation, phosphors with

non-rare earth metals as activators are considered by researchers. For example, Xia's group recently reported an ultra-broad-band white emission phosphor, $(C_6H_{18}N_2O_2)PbBr_4:Mn^{2+}$, ($\lambda_{em}$ = 640 nm; FWHM = 230 nm), but it has low quantum efficiency (about 12.51%) and poor chemical stability due to the existence of small organic molecules [16]. Compared to the activators Eu^{2+}, Ce^{3+} and Mn^{2+} aforementioned, Bi^{3+} has a high probability of achieving white light emission in different host materials, since Bi^{3+} is sensitive to the surrounding crystal field environment, which makes it easy to achieve tunable emission by adjusting the crystal structure [2, 17-19]. In addition, the excitation band of Bi^{3+} is mainly concentrated in the near-UV region, and it barely overlaps with its emission band, which effectively avoids the problem of chromatic aberration caused by reabsorption [6, 20, 21]. Therefore, broadband white light could be realized by adjusting the crystal fields of Bi^{3+} emission centers.

In order to broaden the emission range of Bi^{3+}-doped phosphors, many effective strategies have been adopted: (i) cationic substitution engineering: Xia et al. achieved different emission of Bi^{3+} in $ALa_{0.98}Ta_2O_7:0.02Bi^{3+}$ samples by mutual exchange of Rb, K and Na, corresponding to the emission peaks of 540, 550 and 510 nm, respectively [22]. Similarly, a spectral regulation from 456 nm to 674 nm was obtained by controlling the ratios of Sc/Y and V/Nb in the $(Nb_{1-x},V_x)(Y_{1-y},Sc_y)O_4:Bi^{3+}$ phosphors [23]. (ii) energy transfer engineering: Lin and colleagues conducted energy transfer of Bi^{3+} to Eu^{3+} in $BaSc_2O_4$ host, and announced that the emission color could be successfully adjusted from blue (at 440 nm) to red (at 660 nm) [24]. Other types of

energy transfer such as host → Bi^{3+}, Bi^{3+} → Mn^{4+}, Bi^{3+} → Sm^{3+}, Bi^{3+} → Mn^{2+} and so on have also been proven in which it could tune the emission color [25-30]. (iii) site-selective excitation: based on the previous works by Lei et al., multiple different luminous centers were discovered in $ZnWO_4$ crystal, which resulted in the 498-672 nm emission being monitored under 250-400 nm excitation wavelengths [31]. (iv) Bi^{3+} concentration engineering: the PL spectra may be shifted when Bi^{3+} ions occupy different luminous centers. For example, a red shift of the emission peak from 418 to 462 nm was achieved with the increase of Bi^{3+} concentration in $Ca_5(BO_3)_3F$:$y$$Bi^{3+}$ phosphor [32]. Analogously, the emission color of $Sr_3Ga_4O_9$:Bi^{3+} changes from blue to red area[33]. All in all, the above strategies have crucial guiding significance for obtaining Bi^{3+}-doped broadband white phosphors [6, 34].

In recent years, the K_2MgGeO_4:Bi^{3+} (KMGO:Bi^{3+}) phosphor has been reported, which has a broad band emission with FWHM of 148 nm. For the KMGO structure, there are four different positions (K_1, K_2, K_3 and K_4) for Bi^{3+} to occupy, which may lead to different luminescence properties of Bi^{3+}. However, the occupied state of Bi^{3+} in these four sites has not been studied thoroughly in previous reports [35]. Enlightened by the above reports, we designed the $K_{2-x-y}A_xMgGeO_4$:yBi^{3+} (A = Li, Na and Rb) and investigated the influence of site-selective excitation and Bi^{3+} doping concentration on the Bi^{3+} emission. The results showed that the FWHM is broadened to 204 nm in the $K_{1.456}N_{0.54}$MGO:0.004Bi^{3+} sample under excitation at 320 nm, this behavior was explained due to the generation of new luminous centers and occupied rearrangement of Bi^{3+} in KMGO:Bi^{3+} host caused by alkali metal ions (Li^+, Na^+)

substitution. Moreover, the thermal stability of KMGO:Bi^{3+} was enhanced from 83.97% to 88.66% after Rb^{+} substitution engineering. Finally, the WLED devices with high CRI (R_a = 93.4) can be fabricated by combining the as-prepared phosphor and near-UV chip. This study may open up a new understanding and perspective for designing broadband white phosphors.

2. Experimental section

2.1. Materials synthesis:

$K_{2-x-y}A_xMgGeO_4:yBi^{3+}$ (A = Li, Na and Rb; $0 \leq x \leq 1$) were prepared by using proper amounts of K_2CO_3 (AR), Li_2CO_3 (AR), Na_2CO_3 (AR), Rb_2CO_3 (99.999%), GeO_2 (99.999%), MgO (AR) and Bi_2O_3 (99.999%) as raw materials. All the ingredients were purchased from Aladdin. According to the stoichiometric ratio, the required ingredients were weighted and ground together with 2 mL ethanol for 20 min by hand. Prior to final sintering, the mixtures were pre-fired at 800 °C for 2 h with a heating rate of 2 °C/min, which was followed by grinding for 10 min to blend these powders more fully. After that, the mixtures were sintered again at 1050 °C for 10 h (heating rate of 5 °C/min). Finally, these samples were quenched to room temperature and were reground for consequent measurements. Concretely, take $K_{1.45}N_{0.54}MGO:0.04Bi^{3+}$ as an example, 3.4133 g raw materials (1.2483 g K_2CO_3, 1.2983 g GeO_2, 0.3551 g Na_2CO_3, 0.5 g MgO, 0.0116 g Bi_2O_3) can produce about 2.6149 g products.

2.2. WLED fabrication:

WLED device was fabricated through combining the representative $K_{1.456}N_{0.54}MGO:0.004Bi^{3+}$ phosphor and 330 nm n-UV chip. Typically, the phosphor was evenly blended with epoxy resin A and B (A:B = 2:1), and the gained phosphor-epoxy resin mixture was coated on a n-UV chip. All the epoxy resin were purchased from Guangdong Evergrande New Material Technology Co., Ltd. After that, the obtained device was dried at 120 °C for 3 h. The detailed pc-LED preparation process can refer to Fig. S1. For the convenience of comparison, the $K_{1.996}MGO:0.004Bi^{3+}$ phosphor was manufactured into WLED in the same way. Optical tests, including CCT, R_a, CIE color coordinates and electroluminescence (EL) spectrum of the WLEDs, were collected on an ATA-500 measurement system (Everfine, China).

2.3. Characterization:

Powder XRD of as-prepared samples were measured on a Rigaku D/SHIMADZU-6000 diffractometer equip with Cu-Kα radiation, running from 10° to 80° (scan speed of 6°/min). The data for Rietveld refinement were collected on a D8 Advance diffractometer (Bruker Corporation, Germany) and the phase purity were refined based on the TOPAS 4.2 software. Dualbeam electron microscope (Tescan Mira3) was used to test scanning electron microscope (SEM) images and elemental composition. The X-ray photoelectron spectroscopy (XPS) was obtained on Thermo Scientific K-Alpha+ with an Al Kα source. QE-2100 testing system (Otsuka, Japan) was used to test the quantum efficiency (QE). Under the excitation source of 150 W Xe lamp, the emission and excitation spectra were obtained on a Hitachi F-4700

spectrometer. The same spectrometer combined an Orient KOJI heat controller was used to test temperature-dependent emission spectra. The decay times were measured by an Edinburgh FLS920 spectrometer using a Xe900 lamp.

3. Results and discussion

3.1. Crystal Structure and morphology analysis

The designed compound with chemical formula $K_{2-x}Na_xMgGeO_4:Bi^{3+}$ (abbreviated to $K_{2-x}N_xMGO:Bi^{3+}$ hereafter) is obtained by cation replacement engineering on the basis of $KMGO:Bi^{3+}$. Fig. 1a displays the XRD patterns of $K_{2-x}N_xMGO:Bi^{3+}$ phosphors. When a small amount of Na^+ substitutes for K^+ in the $KMGO:Bi^{3+}$ matrix, all main peaks are almost identical with the calculated XRD patterns, suggesting the successful preparation and phase purity. Impurities begin to appear when more Na^+ ($x > 0.4$) replaces K^+ in the sample. Moreover, Rietveld refinement results show that the impurity belongs to Na_2MgGeO_4 (NMGO) compound and its content increases following the improved substitution level of Na^+. In the phosphor with $x = 0.6$, the maximum amount of impurity is found to be 16.2 wt% (see Fig. S2). Furthermore, $NMGO:Bi^{3+}$ sample was prepared and tested to explore its influence on the main phase luminescence, and the related results are given in Fig. S3. Obviously, there is little overlap in the emission spectrum between $NMGO:Bi^{3+}$ and $K_{2-x}N_xMGO:Bi^{3+}$ ($x = 0$-1). Therefore, when discussing the luminescence properties of $K_{2-x}N_xMGO:Bi^{3+}$, the impurity phase will not interfere with it. In addition, the enlarged XRD pattern in Fig. 1a shows that the strongest diffraction peak at 32.0°

shifts to higher angle direction with the gradual substitution with Na^+. In consideration of $r(K^+) > r(Na^+)$, this phenomenon could be well explained by Bragg's law $2d\sin\theta = n\lambda$ (where λ, θ and d are the diffraction angle and integer, diffraction wavelength and the interplanar crystal spacing, respectively) [17, 27]. Besides, the cell parameters of KMGO:Bi^{3+} are listed as a = 11.19 Å, b = 5.58 Å, c = 15.83 Å and V = 988.20 Å^3, while these parameters in $K_{1.4}N_{0.6}$MGO:Bi^{3+} are a = 11.15 Å, b = 5.56 Å, c = 15.77 Å and V = 977.57 Å^3, which indicates that Na^+ is replaced into the unit cell successfully and lead to the shrinkage of lattice volume. A comparison of the measured and calculated XRD patterns is shown in Fig. 1b and Fig. 1c.

(Inset Fig. 1)

The KMGO crystal belongs to $Pca2_1$ space group with orthorhombic system as displayed in Fig. 1d. The crystal framework of KMGO was constituted of Mg and Ge tetrahedron and K atoms located at the cavities sites. Concretely, GeO_4 and MgO_4 are arranged alternately and connected by their corners to form a cavity. Therein, four kinds of K atoms are located at the cavities, named as K1, K2, K3, and K4 sites. K1 and K4 are coordinated by five oxygen atoms to form [KO_5] hexahedron, respectively. For K2 and K3 atoms, K2 coordinates with the surrounding six oxygens to form [KO_6] octahedron, and K3 coordinates with the eight oxygens to form [KO_8] polyhedron. In most cases, the coordination number of Bi^{3+} ion is usually 5, 6 and 8. Hence, we suggest that, in KMGO host, Bi^{3+} ion could occupy the position of K^+. According to the report of Davolos [35, 36], K^+ and Bi^{3+} have similar ionic radii (radii difference between substituted and doped ions < 30%), regardless of CN = 6 or CN = 8.

However, for K in the environment of CN =5, its radius is quite different from that of Bi^{3+}, so we believe that Bi^{3+} cannot occupy K^+ in [KO_5] hexahedron. Na^+ and K^+ are both alkali metal ions with similar properties and radii (Supplementary Table S1), the replacement between them has been proven to be feasible in many past works [22, 37-39]. Likewise, from the ionic radii and coordination environment point of view, Na^+ would preferentially occupy the K^+ sites. The substitution of Na^+ for K^+ would lead to the structural shrinkage, affects the crystal field environment around Bi^{3+} and tune the optical properties. The specific details will be discussed in the next chapter.

(Inset Fig. 2)

The local morphology and chemical composition of $K_{2-x}N_xMGO:Bi^{3+}$ phosphor were further characterized by SEM and EDS mapping. As displayed in Fig. 2a-e, the average particle size range of the sample was measured to be around 10-20 μm under different magnifications. Besides, these irregularly shaped particles were composed of small agglomerated crystals, just like most of the products that were obtained by high temperature solid reaction. The elemental mapping images show that all the original elements including Na, K, Ge, Mg, and O are homogeneously distributed in the particles (shown in Fig. 2f), without any element aggregation or phase separation, implying that ideal materials were successfully synthesized through alkali metal modulation engineering.

The luminescence properties of Bi are closely related to its valence state, and thus determining the valence state of Bi is crucial to the subsequent discussion [40]. According to the information in Table. S2, the XPS data of $K_{1.996}MGO:Bi^{3+}$ and

$K_{1.456}N_{0.54}MGO:Bi^{3+}$ samples were fitted, as shown in Fig. S4 and Fig. 2g. All samples show two characteristic Bi^{3+} peaks at near 158.2 and 163.5 eV, which correspond to the Bi $4f_{7/2}$ and Bi $4f_{5/2}$, respectively [2, 9]. Therein, the content of Bi^{3+} is calculated as 92.26% and 94.75% in the $K_{1.996}MGO:Bi^{3+}$ and $K_{1.456}N_{0.54}MGO:Bi^{3+}$ phosphors, respectively, implying that Bi^{3+} is dominant in these samples.

3.2. Tunable photoluminescence in Na^+ modulated $KMGO:Bi^{3+}$ phosphors

(Inset Fig. 3)

In order to understand the influence of Na^+ substitution engineering, the luminescence properties of $K_{2-x}N_xMGO:Bi^{3+}$ (x = 0-1) phosphors were investigated in details. Fig. 3a presents the emission spectra of $KMGO:Bi^{3+}$ under the excitation wavelengths of 300-360 nm. The PL spectrum shows a broad emission band peaking at 566 nm, which is attributed to $^3P_1 \rightarrow {}^1S_0$ transition of Bi^{3+}. Moreover, the emission intensity of $KMGO:Bi^{3+}$ increases obviously with the gradual change of the excitation wavelength until λ_{ex} = 330 nm. Furthermore, as Fig. 3b shows, the emission spectrum could be divided into two peaks at 19920 cm^{-1} (502 nm) and 17123 cm^{-1} (584 nm) by the Gaussian fitting, implying that Bi^{3+} occupy two sites in KMGO matrix. According to the previous analysis, Bi^{3+} can occupy two main positions (K2 and K3) to form luminous centers. Thus, crystal field splitting (*Dq*) could be introduced to explain this phenomenon, according to the equation below [38]:

$$Dq = \frac{1}{6} Z e^2 \frac{r^4}{R^5} \quad (1)$$

where *Z* represents the charge of the anion, *e* is electron charge, *r* stands for the radius of the *d* wave function, and *R* represents the bond length. Generally, the weaker the

Dq value is, the shorter the emission wavelength will be. Taking into consideration of the different ionic radii of the two sites (K2, r = 0.138 Å, CN = 6; K3, r = 0.151 Å, CN = 8), it could be inferred that Bi^{3+} ions occupy the K2 and K3 sites that result in the emission peaks at 584 and 502 nm, respectively. Fig. 3c displays that the excitation peaks of KMGO:Bi^{3+} are located at 326.8 and 327.8 nm under the monitoring of 502 and 584 nm. For the most part, different luminescence centers could be identified through measuring the luminescence decay curves. Hence, the decay curve of KMGO:Bi^{3+} is measured and fitted, as shown in Fig. 3d. These data can be fitted through typical double exponential decay model, and specific equations shown below [20]:

$$I_{(t)} = I_0 + A_1 \exp\left(\frac{-t}{\tau_1}\right) + A_2 \exp\left(\frac{-t}{\tau_2}\right) \quad (2)$$

$$\tau^* = \frac{A_1\tau_1{}^2 + A_2\tau_2{}^2}{A_1\tau_1 + A_2\tau_2} \quad (3)$$

where $I_{(t)}$ and I_0 are the luminescence intensity at time t and 0, respectively. A_1 and A_2 stand for constants, τ_1 and τ_2 are exponential components of the decay time, and τ^* stands for the average lifetime. Here, the τ^* for peaks at 502 and 584 nm were calculated to be 0.83 and 1.30 μs, indicating the existence of two luminous centers in KMGO:Bi^{3+}. Furthermore, the intensity comparison of two luminescence centers at different excitation wavelengths is shown in Fig. 3e. The luminescence intensity of Bi^{3+} in six-coordination is significantly higher than in eight-coordination, illustrating the dominance of $Bi_{K2}{}^{3+}$ centers in emission.

(Inset Fig. 4)

In order to evaluate the effect of Na^+ modulation on the photoluminescence

properties, the normalized emission spectra of $K_{1.99-x}N_xMGO:0.01Bi^{3+}$ (x = 0-1) phosphors are measured under the excitation wavelengths of 300-365 nm, as shown in Fig. S5 and Fig. S6. As Na^+ is gradually introduced, the extra emission peak (465 nm) is observed. More importantly, the emission intensity at 566 nm gradually decreases, and the intensity at around 465 nm gradually increases. This result demonstrates that introduction of Na^+ resulted in new luminous centers and reformed the lattice placeholder of Bi^{3+}. Besides, these luminous centers have different responsiveness to different excitation sources. To better understand this phenomenon, Fig. 4a shows the emission spectra of a typical sample ($K_{1.45}N_{0.54}MGO:0.01Bi^{3+}$) under different excitation wavelengths. As the excitation wavelengths are adjust from 300 to 365 nm, the strongest emission peak gradually shifts from 566 nm to 465 nm. In addition to the peak positions, the peak intensities are closely related to the excitation wavelength, and thus the broad spectral emission could be obtained by controlling over site selective excitation. Fig. 4b presents the FWHM of $K_{1.99-x}N_xMGO:0.01Bi^{3+}$ (x = 0-1) phosphors under various excitation wavelengths. The result shows that $K_{1.44}N_{0.54}MGO:0.01Bi^{3+}$ sample gains the widest FWHM (203 nm) under UV excitation at 320 nm, as plotted in Fig. 4c.

In general, adjusting the Bi^{3+} doping concentration is another way to achieve the emission tuning when multiple luminescence centers exist in the hosts [20]. The emission spectra of the $K_{1.46-y}N_{0.54}MGO:yBi^{3+}$ samples with different Bi^{3+} concentrations are measured and shown in Fig. 4d. When excited at 320 nm of the UV light, the emission spectrum showed two emission peaks, located at 465 and 566 nm,

respectively. At low Bi^{3+} doping concentration (x < 0.002), the emission peak at 465 nm is dominant. With the increase of Bi^{3+} concentration, long-wavelength emission intensity begins to increase compared to short-wavelength. When x = 0.004, the intensities of the emission peaks at the two locations are roughly equal. This phenomenon indicates that Bi^{3+} with low doping level prefers occupying the Na^{+} site corresponding to the blue emission，and for higher Bi^{3+} content, the orange-red emission could be assigned to the Bi^{3+} in the K^{+} sites. However, the overall intensity of PL spectrum starts to decrease due to the concentration quenching after the concentration of Bi^{3+} exceeds 0.0015. Based on the average Bi-Bi distances (R_C) and Dexter's theory in $K_{1.46-y}N_{0.54}MGO:yBi^{3+}$ [41, 42], energy transfer among the nearest neighbor ions accounts for the observed concentration quenching (see details in Supplementary Fig. S7). Besides, the optimal FWHM (about 204 nm) is detected when the Bi^{3+} doping concentration reaches 0.004 (see Fig. 4e). Based on Gaussian fitting, Fig. 4f shows that the emission spectrum could be divided into four peaks at 22624 cm^{-1} (442 nm), 20746 cm^{-1} (482 nm), 18416 cm^{-1} (543 nm) and 16694 cm^{-1} (599 nm), respectively. Furthermore, two different excitation spectra were obtained under the monitoring of the above emission peaks, and the excitation peak positions are located at 329 and 340 nm, respectively (see Fig. 4g). Compared with the spectrum of $KMGO:Bi^{3+}$ phosphors, the new luminescence centers are generated after Na^{+} modulation that can be mainly excited by 340 nm light source. Fig. 4h displays the photoluminescence decay curves of the $K_{1.456}N_{0.54}MGO:0.04Bi^{3+}$ sample, and these data are different from the result of $KMGO:Bi^{3+}$, which are more in line with the

third-order exponential decay model, confirming further the fact that the new luminous center was generated. The third-order exponential decay model is expressed as follows [15]:

$$I_{(t)} = A_1 \exp\left(\frac{-t}{\tau_1}\right) + A_2 \exp\left(\frac{-t}{\tau_2}\right) + A_3 \exp\left(\frac{-t}{\tau_3}\right) \quad (4)$$

$$\tau^* = \frac{A_1\tau_1{}^2 + A_2\tau_2{}^2 + A_3\tau_3{}^2}{A_1\tau_1 + A_2\tau_2 + A_3\tau_3} \quad (5)$$

Herein, the lifetimes of the four Gauss peaks were calculated to be 0.47, 0.70, 1.19 and 1.46 μs, respectively. Generally speaking, tunable emission can be realized in KMGO phosphor by using Na^+ substitution engineering combined with site-selective excitation and Bi^{3+} concentration optimization. The CIE chromaticity coordinates diagram and the corresponding photographs of $K_{1.456}N_{0.54}MGO:xBi^{3+}$ phosphors excited at 320 nm and $K_{1.456}N_{0.54}MGO:0.04Bi^{3+}$ phosphor excited at different wavelengths are displayed in Fig. 4i, in which the emission color tuning from orange to blue can be clearly observed.

Fig. 5a,b display the QE measurements of $K_{1.456}N_{0.54}MGO:0.004Bi^{3+}$ and $K_{1.996}MGO:0.004Bi^{3+}$ phosphors and more details were listed in Table. S3. The results show that the influence of the introduction of Na^+ on QE is closely related to the excitation wavelength. Specifically compared with $K_{1.996}MGO:0.004Bi^{3+}$, the introduction of Na^+ could improve the QE under low-energy excitation (λ_{ex} = 340-360 nm). While under high-energy excitation (λ_{ex} = 300-330 nm), it has a counterproductive effect. In summary, the optimal IQE and EQE of $K_{1.45}N_{0.54}MGO:0.04Bi^{3+}$ were determined to be 47.01% and 30.06%, respectively, which still has a certain gap with commercial phosphors. Therefore, the QE of this

phosphor needs to be further improved by eliminating the impurity, controlling the particle size and morphology.

(Inset Fig. 5)

3.3. Universal verification of mechanism

As mentioned above, Na^+ modulation can effectively regulate Bi^{3+} luminescence performance. One may ask, could other alkali metals such as Li^+ and Rb^+ play the same role? To verify this speculation, the corresponding Li^+/Rb^+ substitution samples were prepared and studied. In order to keep the consistency with the previous part, the following takes $K_{1.456}Li_{0.54}MgGeO_4:Bi^{3+}$ ($K_{1.456}L_{0.54}MGO:Bi^{3+}$) and $K_{1.456}Rb_{0.54}MgGeO_4:Bi^{3+}$ ($K_{1.456}R_{0.54}MGO:Bi^{3+}$) as examples for illustration. The emission spectra of $K_{1.456}L_{0.54}MGO:Bi^{3+}$ sample at different excitation wavelengths are shown in Fig. 6a, and the phosphors mainly produce broadband emission with emission peak at 530 nm under the excitation of high energy (300 nm). The emission peak has a gradual blue shifts to 444 nm as the excitation energy decreases to 360 nm, and the FWHM initially increases and then decreases. According to the Gaussian fitting, the emission band of 320 nm excited can be divided into four sub-bands peaking at 425, 479, 542 and 606 nm, respectively (Fig. 6b). The excitation spectra were measured using these Gaussian peaks as the monitoring conditions, as shown in Fig. 6c, and the results show that the excitation spectrum is mainly distributed in two positions at 314 and 370 nm. These phenomena are similar to $K_{1.456}N_{0.54}MGO:Bi^{3+}$, indicating that the Li^+ substitution engineering can also generate new luminous centers. However, the results of Rb^+ modulation are more similar to those of

KMGO:Bi^{3+} (see Fig. 6d-f). The $K_{1.456}R_{0.54}$MGO:Bi^{3+} phosphor exhibits a broad band of a dominant peak at 562 nm under different excitation wavelength. Furthermore, two sub-bands could be obtained by Gaussian fitting of emission spectrum and the excitation spectrum shows the same shape and peak position (334 nm).

(Inset Fig. 6)

By combining the above experimental phenomena and crystal structure, the four luminescence centers can be divided into two types: (1) Bi^{3+} occupies the K1 and K4 sites; (2) Bi^{3+} occupies the K2 and K3 sites. According to the analysis of the crystal structure, Bi^{3+} would be more likely to occupy K2 and K3 sites in the KMGO matrix, corresponding to the emission of 502 and 584 nm. Considering the order $r(Li^+)$ < $r(Na^+)$ < $r(K^+)$ (Supplementary Table S1), when Li^+ or Na^+ replaces K^+ at K1 and K4 sites, Bi^{3+} can occupy the Li^+ or Na^+ with a relatively small radius in these sites, leading to the generation of new luminous center. However, for Rb^+ with $r(Rb^+)$ > $r(K^+)$ (Supplementary Table S1), Bi^{3+} is less likely to occupy Rb^+ at the sites of K1 and K4, which results in the emission spectrum of $K_{1.456}R_{0.54}$MGO:Bi^{3+} similar to KMGO:Bi^{3+}. Fig. 7 is the schematic energy-level diagram of Bi^{3+} in different environment, exhibiting the change of excitation and emission.

(Inset Fig. 7)

3.4. The effect of alkali metal modulation engineering on the thermal stability of KMGO:Bi^{3+}

(Inset Fig. 8)

Normally, high temperature (about 150 ℃) during WLED operation will cause

emission losses because of strong electron-phonon coupling [17, 43-45]. Hence, phosphors with excellent thermal stability is extremely crucial in the application of WLED devices. Based on this requirement, the thermal quenching behaviors of $K_{1.996}MGO:Bi^{3+}$, $K_{1.456}L_{0.54}MGO:Bi^{3+}$, $K_{1.456}N_{0.54}MGO:Bi^{3+}$ and $K_{1.456}R_{0.54}MGO:Bi^{3+}$ phosphors were measured at evaluated temperature from 25 to 200 ℃ under 320 nm excitation, as shown in Fig. 8a and Fig. S8a. The emission peaks of all the samples shift to shorter wavelength with increasing temperature, this blueshift is attributed to the different sensitivity response to temperature for the Bi^{3+} ions at different K^+ sites. Fig. 8b specifically describes the change of peak position and FWHM along with the temperature variation. It is noted that $K_{1.456}L_{0.54}MGO:Bi^{3+}$ and $K_{1.456}N_{0.54}MGO:Bi^{3+}$ show a stronger blueshift compared to $K_{1.996}MGO:Bi^{3+}$ and $K_{1.456}R_{0.54}MGO:Bi^{3+}$, indicating the Li^+ and Na^+ modulation will induce Bi^{3+} to occupy the K1 and K4 sites in the lattice. This phenomenon further validates the feasibility of the previous analysis about the site occupation of Bi^{3+} ions. As for FWHM of the emission bands, except for $K_{1.456}L_{0.54}MGO:Bi^{3+}$, the rest of the samples shrink with the increase of temperature. As given in Fig. 8c, at 150 ℃, the integrated intensity of $K_{1.996}MGO:Bi^{3+}$ remains about 83.97% of the initial intensity at 25 ℃, suggesting robustness towards thermal stability. Specifically, the Rb^+ modulation effectively enhances the thermal stability of the $K_{1.996}MGO:Bi^{3+}$ phosphor (increased about 4.69%), while the introduction of Li^+ and Na^+ has a counterproductive effect. Clearly, the thermal stability of $K_{1.456}L_{0.54}MGO:Bi^{3+}$ is relatively weak, showing a sharp decline in the emission intensity as temperature increases.

For the purpose of studying the thermal quenching phenomenon, the activation energy (E_a) is considered, which could be determined by the Arrhenius equation [9, 46-48]:

$$\ln\left(\frac{I_0}{I_T}-1\right)=\ln A-\frac{E_a}{kT} \quad (6)$$

where I_0 and I_T stand for the integrated emission intensity measured at 298 K and testing temperature, respectively, k = 8.62 × 10^{-5} eV·K^{-1} refers to Boltzmann's constant and A is a constant. By fitting the relationship between $1/kT$ and $\ln(I_0/I_T-1)$, the E_a value of each sample can be obtained (see Fig. S9). Therefore, the values of E_a for $K_{1.996}MGO:Bi^{3+}$, $K_{1.456}L_{0.54}MGO:Bi^{3+}$, $K_{1.456}N_{0.54}MGO:Bi^{3+}$ and $K_{1.456}R_{0.54}MGO:Bi^{3+}$ samples were calculated to be 0.3612, 0.3138, 0.3558 and 0.3914 eV, respectively. This result indicates that the variation of thermal stability is related to activation energy. In order to describe the thermal quenching mechanism, the configurational coordinate diagram is adopted, as plotted in Fig. 8d. As it shows, under the excitation of n-UV light, the Bi^{3+} electrons could be easily jumped from the 6s ground state to the 6p excited states (stage i), via non-radiative relaxation to reach the lowest 6p level (stage ii). Generally, the electrons would go through a radiative transition and return to the 6s ground state to produce a white emission (stage iii). Nevertheless, under high temperature, the electrons can reach the crossing point between the 6s and 6p states by a thermal excitation process (stage iv) and followed by a consecutive non-radiative transition to return to the ground states (stage v), which leads to the luminescence thermal quenching [9]. Specially, E_a is considered to be the energy difference between the crossing point of the 6s and 6p states and the

lowest 6p level. Obviously, smaller E_a makes it easier to reach the crossing point and the thermal quenching occurs. The E_a of KRMGO:Bi^{3+} is larger than that of $K_{1.996}$MGO:Bi^{3+}, $K_{1.456}L_{0.54}$MGO:Bi^{3+} and $K_{1.456}N_{0.54}$MGO:Bi^{3+}, which clarifies the best thermal stability of $K_{1.456}R_{0.54}$MGO:Bi^{3+} among the four phosphors.

By combining with the thermal stability and optical properties of these four samples, $K_{1.456}N_{0.54}$MGO:Bi^{3+} is considered to be the most promising white-emitting phosphor for WLED applications. Therefore, we conducted an additional thermal degradation resistance test on the $K_{1.456}N_{0.54}$MGO:Bi^{3+} phosphor, as shown in Fig. S8a-b. The emission peak shows blue-shifts from 564 to 497 nm, and meanwhile, the FWHM changes from 204 to 175 nm when temperature gradually rises up from 25 to 300 °C. As the $K_{1.456}N_{0.54}$MGO:Bi^{3+} phosphor is cooled back to 25 °C, the emission peak position, intensity, and FWHM can be restored to initial values. Moreover, this reversible photoemission response at least persists after 9 rounds of heating and cooling cycles (see Fig. S8c). These results indicate that $K_{1.456}N_{0.54}$MGO:Bi^{3+} has excellent thermal degradation resistance and no permanent irreversible degradation occurs during heating and cooling.

3.5. CIE chromaticity coordinates and application for WLEDs

(Inset Fig. 9)

Based on the above discussions, the target phosphor exhibits optimal performance under excitation at 320 nm. Nevertheless, owing to the lack of 320 nm commercial near ultraviolet chips, we can only choose 330 nm chips for WLED experiments. The corresponding CIE chromaticity diagram of KAMGO:Bi^{3+} (A = Li,

Na, K and Rb) phosphors and their relevant photographs excited at 330 nm are shown in Fig. 9a. The CIE coordinates of $K_{1.456}N_{0.54}MGO:Bi^{3+}$ phosphor is calculated to be (0.3094, 0.3539), which is the closest to the white region among the four samples. To further appraise the application foreground as WLED phosphor, the $K_{1.456}N_{0.54}MGO:Bi^{3+}$ phosphor was combined with a n-UV chip (330 nm) to fabricate the WLED i. For comparison, the $K_{1.996}MGO:0.004Bi^{3+}$ phosphor was used to fabricate into WLED ii in the same way. Fig. 9b and Fig. 9c display the EL spectra, R_a, CCT value, and the CIE coordinate of the two WLEDs, and the insets show the photographs of the WLED devices. Obviously, $K_{1.456}N_{0.54}MGO:Bi^{3+}$ covers more of the blue and green component in the visible light region than $K_{1.996}MGO:Bi^{3+}$. Under 3.5 V, 20 mA drive current, the R_a value of the WLED i is 93.4, which is superior to the $K_{1.996}MGO:Bi^{3+}$ phosphor (88.8). Here, WLED i emits cool white light with CCT is 6493 K, whereas WLED ii corresponding to the neutral white light (CCT = 4573 K). Furthermore, the CIE color coordinates of the former (0.309, 0.354) is closer to the white emitting position (0.33, 0.33) than those of the latter (0.360, 0.375). Therefore, $K_{1.456}N_{0.54}MGO:Bi^{3+}$ phosphor with the broadband white emission characteristic seems to have a great prospect in burgeoning WLED application which deserves further exploration.

4. Conclusion

In summary, we have adopted an effective strategy to realize luminescence tuning, improve the thermal stability, and obtain an ultra-wide-band single-phase white phosphor. Rietveld refinement confirmed that Bi^{3+} occupied the K2 and K3

cationic sites of KMGO. The variation of decay under different monitoring wavelengths has verified the existence of multiple emission centers in KMGO:Bi^{3+}. Furthermore, the influence of alkali metal substitution on phosphor's properties was studied and investigated. When smaller alkali metal ions (Na^+, Li^+) are introduced in KMGO:Bi^{3+}, additional emission peaks are generated around at 450 nm attributable to the Bi^{3+} occupying the Na^+/Li^+ sites, which forms ultra-broad-band white emission (FWHM = 204 nm). In addition, larger alkali metal ions (Rb^+) cannot achieve similar effects, whereas, Rb^+ modulation can improve the thermal stability from 83.97% to 88.66%. This shift was further ascribed to the increased activation energy from 0.3612 to 0.3914 eV in phosphor. More importantly, the WLED devices with high CRI (R_a = 93.4) can be obtained by combining n-UV chip and $K_{1.456}N_{0.54}$MGO:0.004Bi^{3+} phosphor. The strategy of alkali metal substitution engineering provides a new understanding and possibility for discovering idiosyncratic luminescence behavior in inorganic luminescence field.

Acknowledgements

The authors would like to gratefully acknowledge funds from the National Natural Science Foundation of China (Grant No. 21706060, 51703061, 51974123), the Hunan provincial Engineering Technology Research Center for Optical Agriculture (Grant No. 2018TP2003), the Scientific Research Fund of Hunan Provincial Education Department (19C0903), the Distinguished Youth Foundation of Hunan Province (Grant No. 2020JJ2018) and the Natural Sciences Foundation of Hunan agricultural university, China (Grant No. 19QN11). W.-Y. Wong acknowledges

the financial support from the Hong Kong Research Grants Council (C4006-17G and PolyU 153058/19P), the Hong Kong Polytechnic University (1-ZE1C) and Ms Clarea Au for the Endowed Professorship in Energy (847S).

Appendix A. Supplementary data

Supplementary data to this article can be found online at https://www.journals.elsevier.com/

References

[1] H. Zhu, C.C. Lin, W. Luo, S. Shu, Z. Liu, Y. Liu, J. Kong, E. Ma, Y. Cao, R.S. Liu, X. Chen, Highly efficient non-rare-earth red emitting phosphor for warm white light-emitting diodes, Nat. Commun. 5 (2014) 4312-4321.

[2] Y. Wei, G.C. Xing, K. Liu, G.G. Li, P.P. Dang, S.S. Liang, M. Liu, Z.Y. Cheng, D.Y. Jin, J. Lin, New strategy for designing orangish-red-emitting phosphor via oxygen-vacancy-induced electronic localization, Light: Sci. Appl. 8 (2019) 15-23.

[3] R. Gautier, X.Y. Li, Z.G. Xia, F. Massuyeau, Two-Step Design of a Single-Doped White Phosphor with High Color Rendering, J. Am. Chem. Soc. 139 (2017) 1436-1439.

[4] L. Zhang, B.H. Sun, L.C. Gu, W. Bu, X.Z. Fu, R. Sun, T.Y. Zhou, F.A. Selim, C.P. Wong, H. Chen, Enhanced light extraction of single-surface textured YAG:Ce transparent ceramics for high power white LEDs, Appl. Surf. Sci. 455 (2018) 425-432.

[5] H.X. Liao, M. Zhao, M.S. Molokeev, Q.L. Liu, Z.G. Xia, Learning from a Mineral Structure toward an Ultra-Narrow-Band Blue-Emitting Silicate Phosphor RbNa3 $(Li_3SiO_4)_4:Eu^{2+}$, Angew. Chem., Int. Ed. Engl. 57 (2018) 11728-11731.

[6] P.P. Dang, D.J. Liu, G.G. Li, A.A. Al Kheraif, J. Lin, Recent Advances in Bismuth Ion-Doped Phosphor Materials: Structure Design, Tunable Photoluminescence Properties, and Application in White LEDs, Adv. Opt. Mater. 8 (2020) 1901993-1902025.

[7] S.M. Gu, M. Xia, C. Zhou, Z.H. Kong, M.S. Molokeev, L. Liu, W.Y. Wong, Z. Zhou, Red shift properties, crystal field theory and nephelauxetic effect on Mn^{4+}-doped $SrMgAl_{10-y}Ga_yO_{17}$ red phosphor for plant growth LED light, Chem. Eng. J. 396 (2020) 125208-125217.

[8] S.X. Li, Y.H. Xia, M. Amachraa, N.T. Hung, Z.B. Wang, S.P. Ong, R.J. Xie, Data-Driven Discovery of Full-Visible-Spectrum Phosphor, Chem. Mater. 31 (2019) 6286-6294.

[9] D.J. Liu, X.H. Yun, P.P. Dang, H.Z. Lian, M.M. Shang, G.G. Li, J. Lin,

Yellow/Orange-Emitting $ABZn_2Ga_2O_7:Bi^{3+}$(A = Ca, Sr; B = Ba, Sr) Phosphors: Optical Temperature Sensing and White Light-Emitting Diode Applications, Chem. Mater. 32 (2020) 3065-3077.

[10] Z.W. Long, Y.G. Wen, J.H. Zhou, J.B. Qiu, H. Wu, X.H. Xu, X. Yu, D.C. Zhou, J. Yu, Q. Wang, No-Interference Reading for Optical Information Storage and Ultra-Multiple Anti-Counterfeiting Applications by Designing Targeted Recombination in Charge Carrier Trapping Phosphors, Adv. Opt. Mater. 7 (2019) 1900006-1900016.

[11] P.P. Dai, S.P. Lee, T.S. Chan, C.H. Huang, Y.W. Chiang, T.M. Chen, $Sr_3Ce(PO_4)_3:Eu^{2+}$: a broadband yellow-emitting phosphor for near ultraviolet-pumped white light-emitting devices, J. Mater. Chem. C 4 (2016) 1170-1177.

[12] T. Hasegawa, S.W. Kim, T. Ueda, T. Ishigaki, K. Uematsu, H. Takaba, K.J. Toda, M. Sato, Unusual, broad red emission of novel Ce^{3+}-activated $Sr_3Sc_4O_9$ phosphors under visible-light excitation, J. Mater. Chem. C 5 (2017) 9472-9478.

[13] Q.Q. Zhu, L. Wang, N. Hirosaki, L.Y. Hao, X. Xu, R.J. Xie, Extra-Broad Band Orange-Emitting Ce^{3+}-Doped $Y_3Si_5N_9O$ Phosphor for Solid-State Lighting: Electronic, Crystal Structures and Luminescence Properties, Chem. Mater. 28 (2016) 4829-4839.

[14] Z.F. Wang, F.L. Yuan, X.H. Li, Y.C. Li, H.Z. Zhong, L.Z. Fan, S.H. Yang, 53% Efficient Red Emissive Carbon Quantum Dots for High Color Rendering and Stable Warm White-Light-Emitting Diodes, Adv. Mater. 29 (2017) 1702910-1702916.

[15] Z.G. Xia, A. Meijerink, Ce^{3+}-Doped garnet phosphors: composition modification, luminescence properties and applications, Chem. Soc. Rev. 46 (2017) 275-299.

[16] G.J. Zhou, X.X. Jiang, M.S. Molokeev, Z.S. Lin, J. Zhao, J. Wang, Z.G. Xia, Optically Modulated Ultra-Broad-Band Warm White Emission in Mn^{2+}-Doped $(C_6H_{18}N_2O_2)PbBr_4$ Hybrid Metal Halide Phosphor, Chem. Mater. 31 (2019) 5788-5795.

[17] F.W. Kang, M.Y. Peng, D.Y. Lei, Q.Y. Zhang, Recoverable and Unrecoverable Bi^{3+}-Related Photoemissions Induced by Thermal Expansion and Contraction in $LuVO_4:Bi^{3+}$ and $ScVO_4:Bi^{3+}$ Compounds, Chem. Mater. 28 (2016) 7807-7815.

[18] P. Boutinaud, Revisiting the spectroscopy of the Bi^{3+} ion in oxide compounds, Inorg. Chem. 52 (2013) 6028-6038.

[19] R. Hu, Y. Zhang, Y.Y. Zhao, X.S. Wang, G.R. Li, C.Y. Wang, UV–Vis-NIR broadband-photostimulated luminescence of $LiTaO_3:Bi^{3+}$ long-persistent phosphor and the optical storage properties, Chem. Eng. J. 392 (2020) 124807-124818.

[20] Y. Wei, Z.Y. Gao, X.H. Yun, H. Yang, Y.X. Liu, G.G. Li, Abnormal Bi^{3+}-Activated NIR Emission in Highly Symmetric $XAl_{12}O_{19}$ (X = Ba, Sr, Ca) by Selective Sites Occupation, Chem. Mater. 32 (2020) 8747-8753.

[21] T. Wang, X.H. Xu, D.C. Zhou, Y. Yang, J.B. Qiu, X. Yu, Effect of Defect Distribution on the Optical Storage Properties of Strontium Gallates with a Low-Dimensional Chain Structure, Inorg. Chem. 55 (2016) 894-901.

[22] G.J. Zhou, X.X. Jiang, J. Zhao, M.S. Molokeev, Z.S. Lin, Q.L. Liu, Z.G. Xia, Two-Dimensional-Layered Perovskite $ALaTa_2O_7:Bi^{3+}$ (A = K and Na) Phosphors with Versatile Structures and Tunable Photoluminescence, ACS Appl. Mater. Interfaces 10 (2018) 24648-24655.

[23] F.W. Kang, H.S. Zhang, L. Wondraczek, X.B. Yang, Y. Zhang, D.Y. Lei, M.Y. Peng, Band-Gap Modulation in Single Bi^{3+}-Doped Yttrium–Scandium–Niobium Vanadates for Color Tuning over the Whole Visible Spectrum, Chem. Mater. 28 (2016) 2692-2703.

[24] P.P. Dang, S.S. Liang, G.G. Li, Y. Wei, Z.Y. Cheng, H.Z. Lian, M.M. Shang, S.J. Ho, J. Lin, Controllable optical tuning and improvement in Li^{+},Eu^{3+}-codoped $BaSc_2O_4:Bi^{3+}$ based on energy transfer and charge compensation, J. Mater. Chem. C 6 (2018) 6449-6459.

[25] H.P. Zhou, Q.P. Wang, Y. Jin, Temperature dependence of energy transfer in tunable white light-emitting phosphor $BaY_2Si_3O_{10}:Bi^{3+}$,Eu^{3+} for near UV LEDs, J. Mater. Chem. C 3 (2015) 11151-11162.

[26] A. Huang, Z.W. Yang, C.Y. Yu, Z.Z. Chai, J.B. Qiu, Z.G. Song, Tunable and White Light Emission of a Single-Phased $Ba_2Y(BO_3)_2Cl:Bi^{3+}$,Eu^{3+} Phosphor by Energy Transfer for Ultraviolet Converted White LEDs, J. Phys. Chem. C 121 (2017) 5267-5276.

[27] F.W. Kang, M.Y. Peng, X. Yang, B., G.P. Dong, G.C. Nie, W.J. Liang, S.H. Xu, J.R. Qiu, Broadly tuning Bi^{3+} emission via crystal field modulation in solid solution compounds $(Y,Lu,Sc)VO_4$:Bi for ultraviolet converted white LEDs, J. Mater. Chem. C 2 (2014) 6068-6076.

[28] Z. Zhou, Y. Zhong, M. Xia, N. Zhou, B.F. Lei, J. Wang, F.F. Wu, Tunable dual emission of $Ca_3Al_4ZnO_{10}:Bi^{3+}$,Mn^{4+} via energy transfer for indoor plant growth lighting, J. Mater. Chem. C 6 (2018) 8914-8922.

[29] Z.C. Zhang, C.G. Ma, R. Gautier, M.S. Molokeev, Q.L. Liu, Z.G. Xia, Structural Confinement toward Giant Enhancement of Red Emission in Mn^{2+}-Based Phosphors, Adv. Funct. Mater. 28 (2018) 1804150-1804156.

[30] J. Yang, Y.Y. Zhao, Y.Q. Meng, H.C. Zhu, D.T. Yan, C.G. Liu, C.S. Xu, H. Zhang, L. Xu, Y.X. Li, Y.X. Liu, Irradiation-free photodynamic therapy in vivo induced by enhanced deep red afterglow within NIR-I bio-window, Chem. Eng. J. 387 (2020) 124067-124081.

[31] J. Han, L.J. Li, M.Y. Peng, B.L. Huang, F.J. Pan, F.W. Kang, L.Y. Li, J. Wang, B.F. Lei, Toward Bi^{3+} Red Luminescence with No Visible Reabsorption through Manageable Energy Interaction and Crystal Defect Modulation in Single Bi^{3+}-Doped $ZnWO_4$ Crystal, Chem. Mater. 29 (2017) 8412-8424.

[32] X. Li, Z.J. Wang, J.J. Liu, X.Y. Meng, K.L. Qiu, Q. Bao, Y.B. Li, Z.P. Wang, Z.P. Yang, P.L. Li, Mechanism of Crystal Structure Transformation and Abnormal Reduction in $Ca_{5-y}(BO_3)_{3-x}(PO_4)_xF(CBP_xF):yBi^{3+}$, Inorg. Chem. 57 (2018) 13783-13799.

[33] X. Wang, P. Boutinaud, L.Y. Li, J.K. Cao, P.X. Xiong, X.Y. Li, H.Y. Luo, M.Y. Peng, Novel persistent and tribo-luminescence from bismuth ion pairs doped strontium gallate, J. Mater. Chem. C 6 (2018) 10367-10375.

[34] A. Yousif, R.M. Jafer, S. Som, H.C. Swart, The effect of the host lattice on the optical properties of Bi^{3+}in $Ca_{1-x}O$:Bi and $Ca_{1-x}(OH)_2$:Bi phosphors, Appl. Surf. Sci. 433 (2018) 155-159.

[35] H.M. Li, R. Pang, G.Y. Liu, W.Z. Sun, D. Li, L.H. Jiang, S. Zhang, C.Y. Li, J. Feng, H.J. Zhang, Synthesis and Luminescence Properties of Bi^{3+}-Activated K_2MgGeO_4: A Promising High-Brightness Orange-Emitting Phosphor for WLEDs Conversion, Inorg. Chem. 57 (2018) 12303-12311.

[36] A.M. Pires, M.R. Davolos, Luminescence of europium (III) and manganese (II) in barium and zinc orthosilicate, Chem. Mater. 13 (2001) 21-27.

[37] M. Zhao, Z.G. Xia, X.X. Huang, L.X. Ning, R. Gautier, M.S. Molokeev, Y.Y. Zhou, Y.C. chuang, Q.Y. Zhang, Q.L. Liu, K.R. Poeppelmeier, Li substituent tuning of LED phosphors with enhanced efficiency, tunable photoluminescence, and improved thermal stability, Sci. Adv. 5 (2019) 363-369.

[38] M.Y. Chen, Z.G. Xia, M.S. Molokeev, C.C. Lin, C.C. Su, Y.C. Chuang, Q.L. Liu, Probing Eu^{2+} Luminescence from Different Crystallographic Sites in $Ca_{10}M(PO_4)_7$:Eu^{2+} (M = Li, Na, and K) with β-$Ca_3(PO_4)_2$-Type Structure, Chem. Mater. 29 (2017) 7563-7570.

[39] M. Zhao, H.X. Liao, M.S. Molokeev, Y.Y. Zhou, Q.Y. Zhang, Q.L. Liu, Z.G. Xia, Emerging ultra-narrow-band cyan-emitting phosphor for white LEDs with enhanced color rendition, Light: Sci. Appl. 8 (2019) 38-46.

[40] D.J. Liu, X.H. Yun, G.G. Li, P.P. Dang, M.S. Molokeev, H.Z. Lian, M.M. Shang, J. Lin, Enhanced Cyan Emission and Optical Tuning of $Ca_3Ga_4O_9$:Bi^{3+} for High-Quality Full-Spectrum White Light-Emitting Diodes, Adv. Opt. Mater. (2020) 2001037-2001048.

[41] Blasse, G. Energy transfer in oxidic phosphors, Philips Res. Rep. 24 (1969) 131-144..

[42] Dexter, D. L. A Theory of Sensitized Luminescence in Solids, J. Chem. Phys. 21 (1953) 836-850.

[43] Y.H. Kim, P. Arunkumar, B.Y. Kim, S. Unithrattil, E. Kim, S.H. Moon, J.Y. Hyun, K.H. Kim, D. Lee, J.S. Lee, W.B. Im, A zero-thermal-quenching phosphor, Nat. Mater. 16 (2017) 543-550.

[44] S.J. Gai, H.F. Zhu, P.X. Gao, C. Zhou, Z.H. Kong, M.S. Molokeev, Z.Y. Qi, Z. Zhou, M. Xia, Structure analysis, tuning photoluminescence and enhancing thermal stability on Mn^{4+}-doped $La_{2-x}Y_xMgTiO_6$ red phosphor for agricultural lighting, Ceram. Int. 46 (2020) 20173-20182.

[45] Y.Q. Wu, S.S. Zhou, T. He, X.Y. Jin, L.Y. Lun, Photocatalytic activities of $ZnWO_4$ and Bi@$ZnWO_4$ nanorods, Appl. Surf. Sci. 484 (2019) 409-413.

[46] Y. Zhong, S.J. Gai, M. Xia, S.M. Gu, Y.L. Zhang, X.B. Wu, J. Wang, N. Zhou, Z. Zhou, Enhancing quantum efficiency and tuning photoluminescence properties in far-red-emitting phosphor $Ca_{14}Ga_{10}Zn_6O_{35}$:Mn^{4+} based on chemical unit engineering, Chem. Eng. J. 374 (2019) 381-391.

[47] M. Jain, Manju, A. Gundimeda, S. Kumar, G. Gupta, S.O. Won, K.H. Chae, A. Vij, A. Thakur, Defect induced broadband visible to near-infrared luminescence in $ZnAl_2O_4$ nanocrystals, Appl. Surf. Sci. 480 (2019) 945-950.

[48] P. Dai, Q. Wang, M. Xiang, T.-M. Chen, X. Zhang, Y.-W. Chiang, T.-S. Chan, X. Wang, Composition-driven anionic disorder-order transformations triggered single-Eu^{2+}-converted high-color-rendering white-light phosphors, Chem. Eng. J. 380 (2020) 122508-122518.

Figures Captions

Fig. 1. (a) XRD patterns of as-synthesized $K_{2-x}N_xMGO:0.04Bi^{3+}$ (x = 0-0.6) phosphors, the right in figure shows the enlarged XRD pattern between 2θ range of 31.5°-33°; (b)-(c) XRD patterns of $K_{1.996}MGO_4:Bi^{3+}$ and $K_{1.456}N_{0.54}MGO_4:Bi^{3+}$ sample; (d) The crystal structure of KMGO compound and the preferential site occupancy of Bi^{3+} and Na^+.

Fig. 2. (a)-(e) SEM images of $K_{1.456}N_{0.54}MGO:Bi^{3+}$ phosphor with various detecting scales; (f) elemental maps of characteristic particle of $K_{1.456}N_{0.54}MGO:Bi^{3+}$ phosphor; (g) XPS analysis of the Bi 4f orbital for the $K_{1.456}N_{0.54}MGO:Bi^{3+}$ phosphor.

Fig. 3. (a) Emission spectra of $K_{1.996}MGO:0.004Bi^{3+}$ sample under corresponding excitation wavelengths; (b) emission spectrum of $K_{1.996}MGO:0.004Bi^{3+}$ under 320 nm excitation and the Gaussian peaks fitting the emission spectrum of this sample; (c) excitation spectra of $K_{1.996}MGO:0.004Bi^{3+}$ sample monitoring at 502 and 584 nm; (d) the decay curves of $K_{1.996}MGO:0.004Bi^{3+}$ under excitation at 320 nm monitored at different wavelengths; (e) the emission intensity of Bi^{3+} at the two cation sites in $K_{1.996}MGO:0.004Bi^{3+}$ under different excitation wavelengths.

Fig. 4. (a) Emission spectra of $K_{1.45}N_{0.54}MGO:0.01Bi^{3+}$ sample under different excitation wavelengths; (b) the FWHM and emission intensity of $K_{1.99-x}N_xMGO:0.01Bi^{3+}$ (x = 0.4-0.62) samples under various excitation; emission spectra of (c) $K_{1.99-x}N_xMGO:0.01Bi^{3+}$ (x = 0-1) and (d) $K_{1.46-y}N_{0.54}MGO:yBi^{3+}$ (y = 0.0005-0.014) samples under 320 nm excitation; (e) the FWHM and emission intensity of $K_{1.46-y}N_{0.54}MGO:yBi^{3+}$ (y = 0.0005-0.014) samples under 320 nm

excitation; (f) the Gaussian fitting of emission spectra of $K_{1.456}N_{0.54}MGO:0.004Bi^{3+}$ under 320 nm excitation; (g) excitation spectra of $K_{1.456}N_{0.54}MGO:0.004Bi^{3+}$ sample monitoring at 442, 482 543 and 599 nm; (h) the decay curves of $K_{1.456}N_{0.54}MGO:0.004Bi^{3+}$ under excitation at 320 nm monitored at different wavelengths; (i) The CIE chromaticity coordinates and corresponding luminescence photos of $K_{1.46-y}N_{0.54}MGO:yBi^{3+}$ (y = 0.0005-0.014) samples under 320 nm excitation and $K_{1.456}N_{0.54}MGO:0.004Bi^{3+}$ sample under different excitation wavelengths.

Fig. 5. The measurements of QE of (a) $K_{1.456}N_{0.54}MGO:0.004Bi^{3+}$ and (b) $K_{1.996}MGO:0.004Bi^{3+}$ phosphors under different excitation wavelength, the inset is the enlarged pattern range from 400 nm to 700 nm.

Fig. 6. Emission spectra of (a) $K_{1.456}L_{0.54}MGO:0.004Bi^{3+}$ and (d) $K_{1.456}R_{0.54}MGO:0.004Bi^{3+}$ samples under corresponding excitation wavelengths; the Gaussian fitting of emission spectra of (b) $K_{1.456}L_{0.54}MGO:0.004Bi^{3+}$ and (e) $K_{1.456}R_{0.54}MGO:0.004Bi^{3+}$ samples under 320 nm excitation; excitation spectra of (c) $K_{1.456}L_{0.54}MGO:0.004Bi^{3+}$ and (f) $K_{1.456}R_{0.54}MGO:0.004Bi^{3+}$ samples monitored at different wavelengths.

Fig. 7. Schematic energy level diagram for Bi^{3+} ions in the $K_{1.456}A_{0.54}MGO:0.004Bi^{3+}$ (A = Li, Na, K and Rb) crystal structures.

Fig. 8. Temperature-dependent PL spectral from 25 to 200 ℃ for $K_{1.456}A_{0.54}MGO:0.004Bi^{3+}$ (A = Li, K and Rb); (b) FWHM and peak position as a function of temperature, (c) Normalized emission intensity of $K_{1.456}A_{0.54}MGO:0.004Bi^{3+}$ (A = Li, Na, K and Rb); (d) configurational coordinate

diagram for Bi^{3+} ions in different phosphors.

Fig. 9. (a) CIE color coordinates and digital photos of $K_{1.456}A_{0.54}MGO:0.004Bi^{3+}$ (A = Li, Na, K and Rb) phosphors; Electroluminescent spectrum and digital photos of WLED that were fabricated from (b) $K_{1.456}N_{0.54}MGO:Bi^{3+}$ and (C) $K_{1.996}MGO:Bi^{3+}$ phosphor with a 330 nm LED chip.

Fig.1

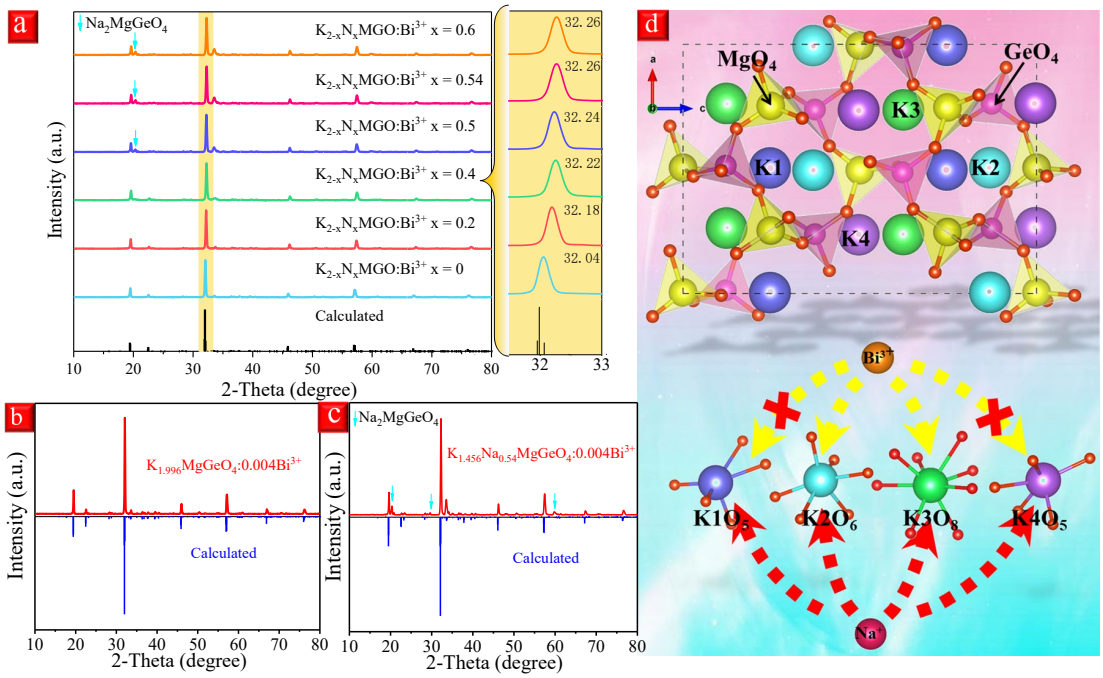
a
Na2MgGeO4
K2-xNxMGO:Bi3+ x = 0.6
K2-xNxMGO:Bi3+ x = 0.54
K2-xNxMGO:Bi3+ x = 0.5
K2-xNxMGO:Bi3+ x = 0.4
K2-xNxMGO:Bi3+ x = 0.2
K2-xNxMGO:Bi3+ x = 0
Calculated
Intensity (a.u.)
2-Theta (degree)
32. 26
32. 26
32. 24
32. 22
32. 18
32. 04
b
K1.996MgGeO4:0.004Bi3+
Calculated
Intensity (a.u.)
2-Theta (degree)
c
Na2MgGeO4
K1.456Na0.54MgGeO4:0.004Bi3+
Calculated
Intensity (a.u.)
2-Theta (degree)
d
MgO4
GeO4
K1
K2
K3
K4
Bi3+
K1O5
K2O6
K3O8
K4O5
Na+

Fig.2

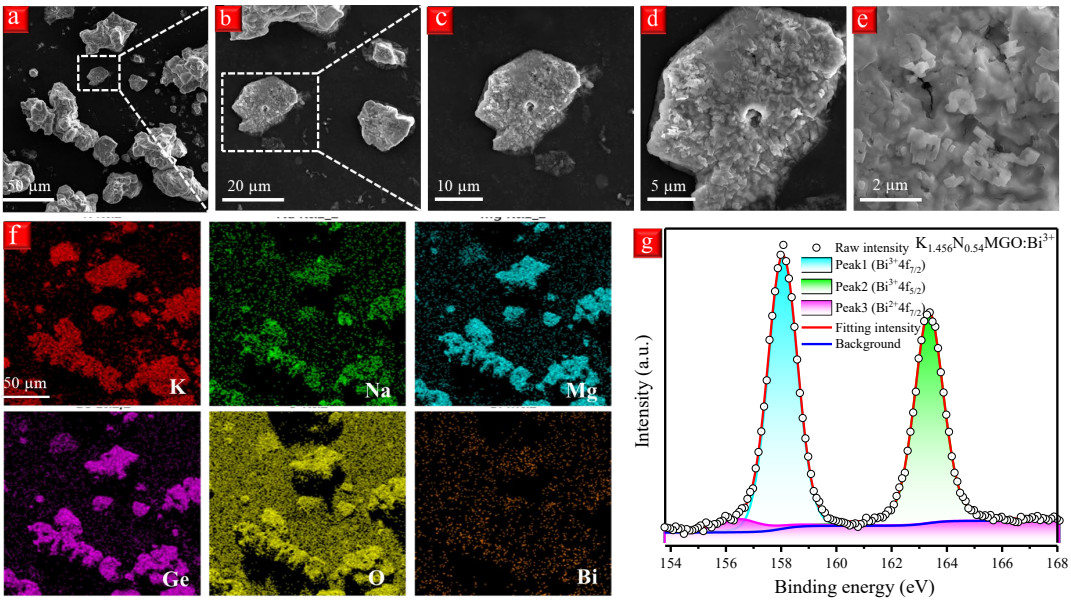
a
50 μm
b
20 μm
c
10 μm
d
5 μm
e
2 μm
f
50 μm
K
Na
Mg
Ge
O
Bi
g
Raw intensity
Peak1 (Bi3+4f7/2)
Peak2 (Bi3+4f5/2)
Peak3 (Bi2+4f7/2)
Fitting intensity
Background
K1.456N0.54MGO:Bi3+
Intensity (a.u.)
154
156
158
160
162
164
166
168
Binding energy (eV)

Fig.3

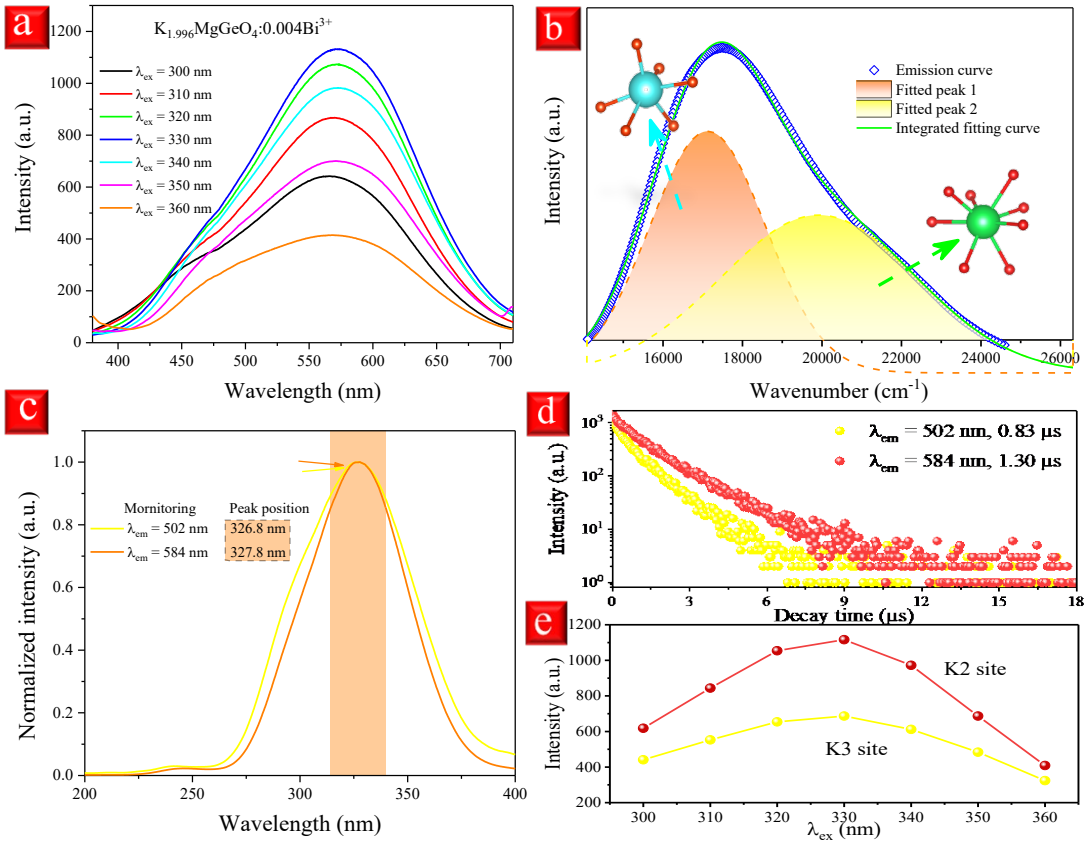
a
$K_{1.996}MgGeO_4$:0.004Bi^{3+}
λ_{ex} = 300 nm
λ_{ex} = 310 nm
λ_{ex} = 320 nm
λ_{ex} = 330 nm
λ_{ex} = 340 nm
λ_{ex} = 350 nm
λ_{ex} = 360 nm
Intensity (a.u.)
Wavelength (nm)
b
Emission curve
Fitted peak 1
Fitted peak 2
Integrated fitting curve
Intensity (a.u.)
Wavenumber (cm^{-1})
c
Mornitoring
Peak position
λ_{em} = 502 nm
326.8 nm
λ_{em} = 584 nm
327.8 nm
Normalized intensity (a.u.)
Wavelength (nm)
d
λ_{em} = 502 nm, 0.83 μs
λ_{em} = 584 nm, 1.30 μs
Intensity (a.u.)
Decay time (μs)
e
K2 site
K3 site
Intensity (a.u.)
λ_{ex} (nm)

Fig.4

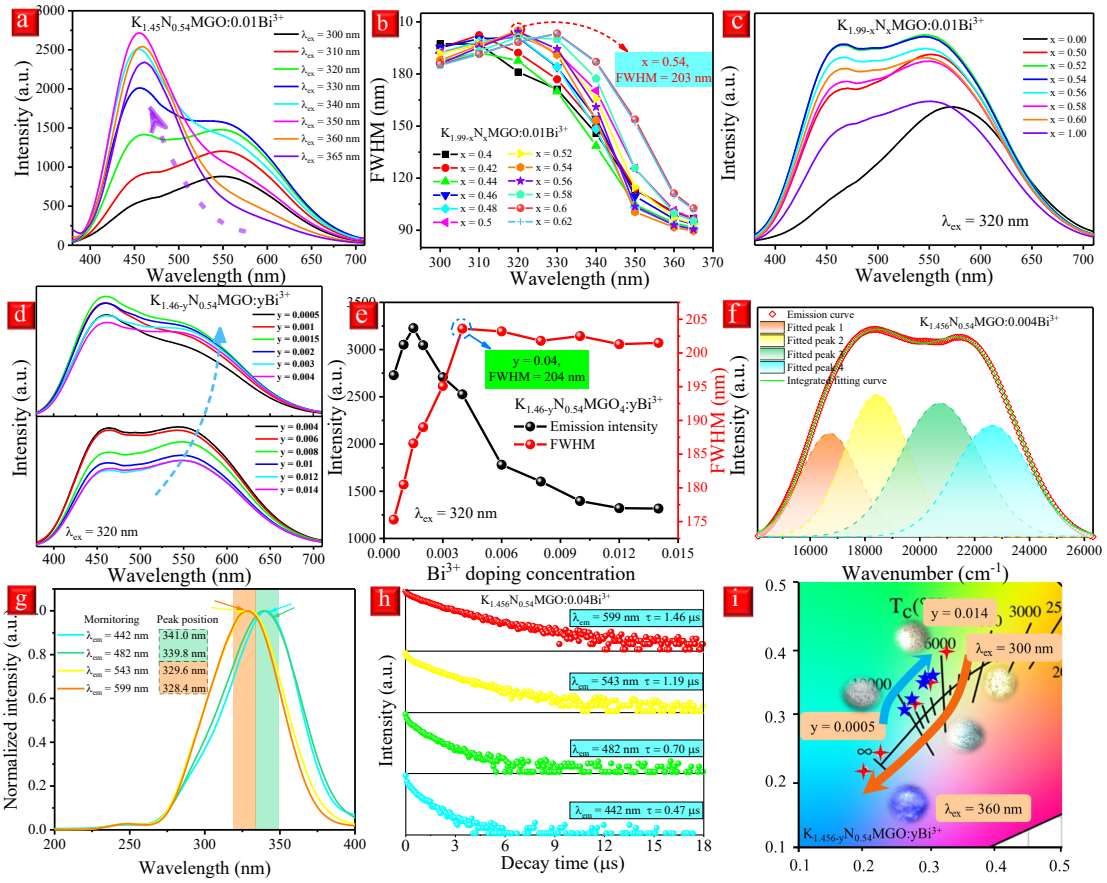
a
$K_{1.45}N_{0.54}MGO:0.01Bi^{3+}$
Intensity (a.u.)
Wavelength (nm)
b
FWHM (nm)
x = 0.54, FWHM = 203 nm
$K_{1.99-x}N_xMGO:0.01Bi^{3+}$
Wavelength (nm)
c
$K_{1.99-x}N_xMGO:0.01Bi^{3+}$
Intensity (a.u.)
λ_{ex} = 320 nm
Wavelength (nm)
d
$K_{1.46-y}N_{0.54}MGO:yBi^{3+}$
Intensity (a.u.)
λ_{ex} = 320 nm
Wavelength (nm)
e
y = 0.04, FWHM = 204 nm
$K_{1.46-y}N_{0.54}MGO_4:yBi^{3+}$
Emission intensity
FWHM
Intensity (a.u.)
FWHM (nm)
λ_{ex} = 320 nm
Bi^{3+} doping concentration
f
Emission curve
Fitted peak 1
Fitted peak 2
Fitted peak 3
Fitted peak 4
Integrated fitting curve
$K_{1.456}N_{0.54}MGO:0.004Bi^{3+}$
Intensity (a.u.)
Wavenumber (cm^{-1})
g
Mornitoring
Peak position
λ_{em} = 442 nm 341.0 nm
λ_{em} = 482 nm 339.8 nm
λ_{em} = 543 nm 329.6 nm
λ_{em} = 599 nm 328.4 nm
Normalized intensity (a.u.)
Wavelength (nm)
h
$K_{1.456}N_{0.54}MGO:0.04Bi^{3+}$
λ_{em} = 599 nm τ = 1.46 μs
λ_{em} = 543 nm τ = 1.19 μs
λ_{em} = 482 nm τ = 0.70 μs
λ_{em} = 442 nm τ = 0.47 μs
Intensity (a.u.)
Decay time (μs)
i
y = 0.014
y = 0.0005
λ_{ex} = 300 nm
λ_{ex} = 360 nm
$K_{1.456-y}N_{0.54}MGO:yBi^{3+}$

Fig.5

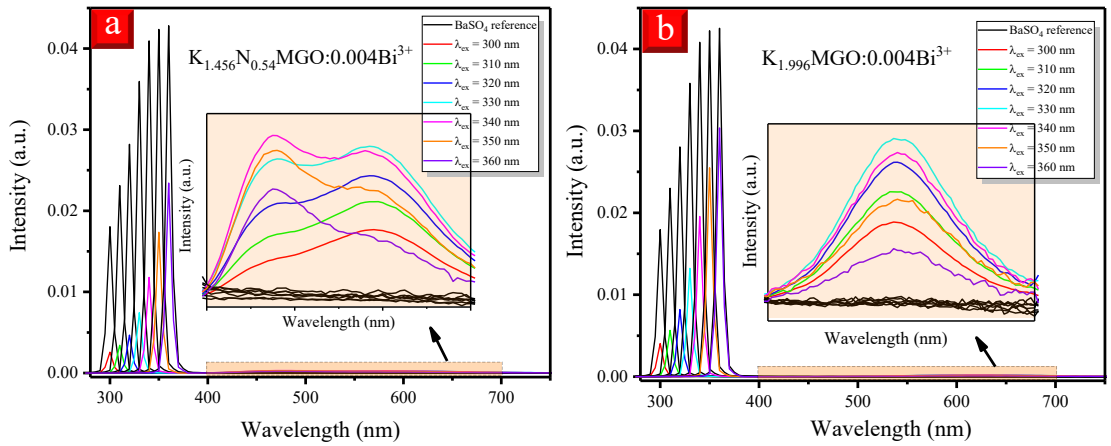
a
$K_{1.456}N_{0.54}MGO:0.004Bi^{3+}$
BaSO4 reference
λex = 300 nm
λex = 310 nm
λex = 320 nm
λex = 330 nm
λex = 340 nm
λex = 350 nm
λex = 360 nm
Intensity (a.u.)
Wavelength (nm)
b
$K_{1.996}MGO:0.004Bi^{3+}$
BaSO4 reference
λex = 300 nm
λex = 310 nm
λex = 320 nm
λex = 330 nm
λex = 340 nm
λex = 350 nm
λex = 360 nm
Intensity (a.u.)
Wavelength (nm)

Fig.6

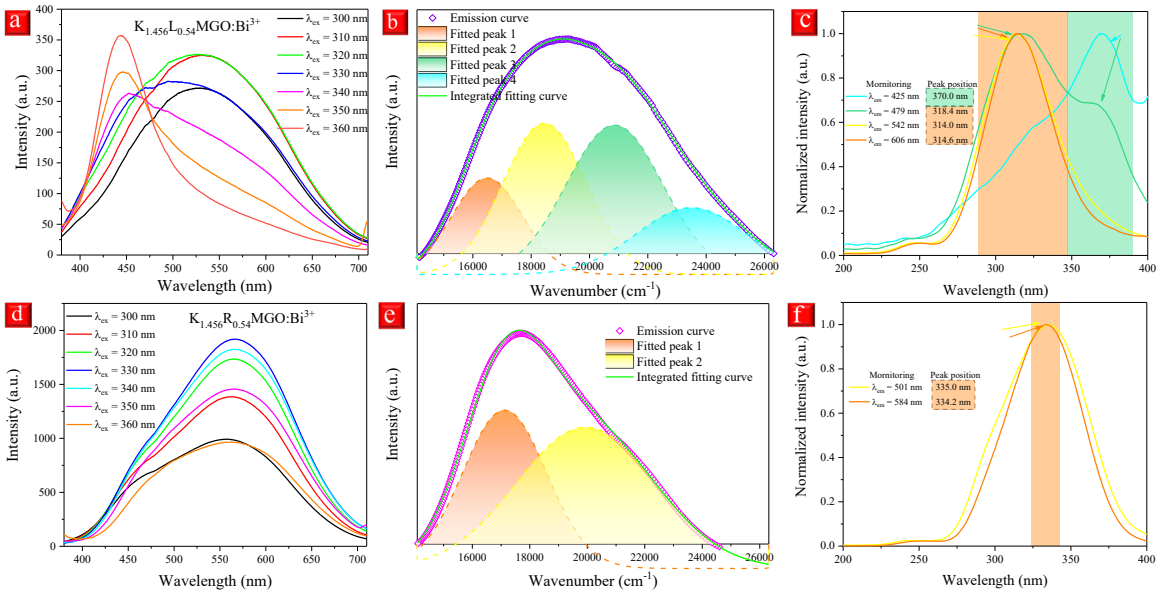
a
$K_{1.456}L_{0.54}MGO:Bi^{3+}$
λ_{ex} = 300 nm
λ_{ex} = 310 nm
λ_{ex} = 320 nm
λ_{ex} = 330 nm
λ_{ex} = 340 nm
λ_{ex} = 350 nm
λ_{ex} = 360 nm
Intensity (a.u.)
Wavelength (nm)
b
Emission curve
Fitted peak 1
Fitted peak 2
Fitted peak 3
Fitted peak 4
Integrated fitting curve
Intensity (a.u.)
Wavenumber (cm^{-1})
c
Mornitoring
Peak position
λ_{em} = 425 nm
370.0 nm
λ_{em} = 479 nm
318.4 nm
λ_{em} = 542 nm
314.0 nm
λ_{em} = 606 nm
314.6 nm
Normalized intensity (a.u.)
Wavelength (nm)
d
$K_{1.456}R_{0.54}MGO:Bi^{3+}$
λ_{ex} = 300 nm
λ_{ex} = 310 nm
λ_{ex} = 320 nm
λ_{ex} = 330 nm
λ_{ex} = 340 nm
λ_{ex} = 350 nm
λ_{ex} = 360 nm
Intensity (a.u.)
Wavelength (nm)
e
Emission curve
Fitted peak 1
Fitted peak 2
Integrated fitting curve
Intensity (a.u.)
Wavenumber (cm^{-1})
f
Mornitoring
Peak position
λ_{em} = 501 nm
335.0 nm
λ_{em} = 584 nm
334.2 nm
Normalized intensity (a.u.)
Wavelength (nm)

Fig.7

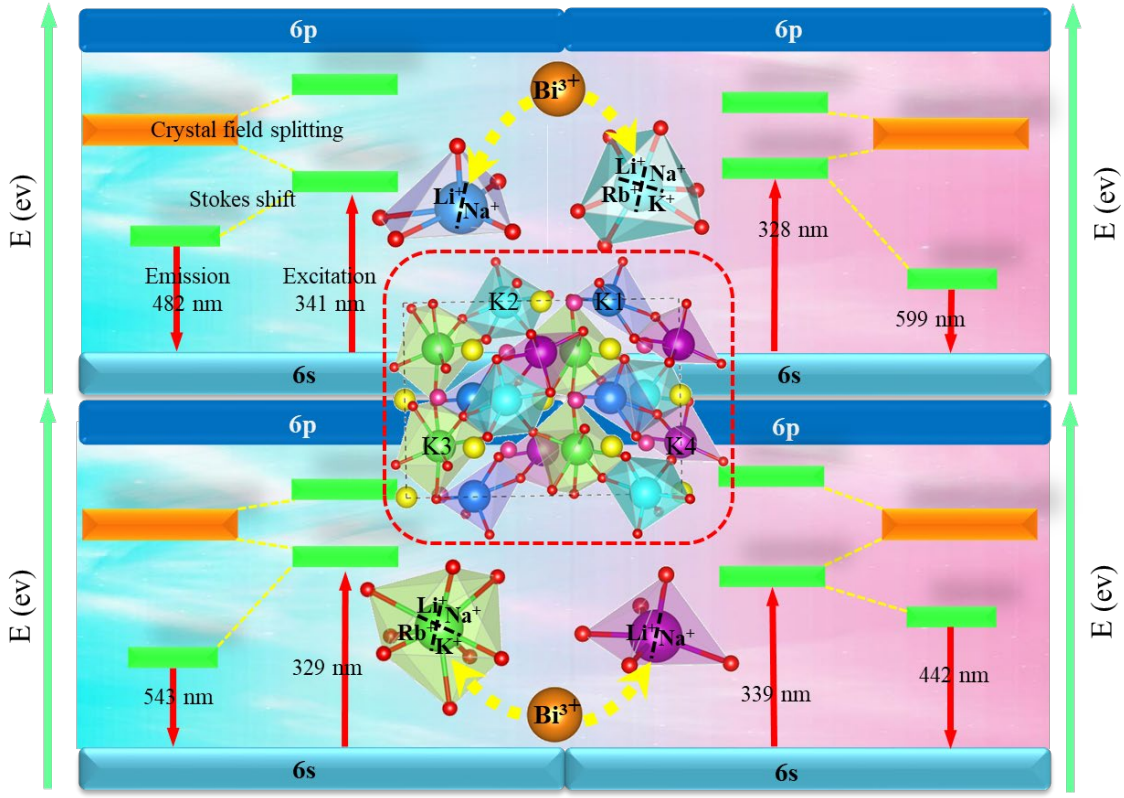
6p
6p
Bi3+
Crystal field splitting
Stokes shift
Emission
482 nm
Excitation
341 nm
Li+Na+
Li+Na+Rb+K+
328 nm
599 nm
E (ev)
E (ev)
6s
6s
K2
K1
K3
K4
6p
6p
Li+Na+Rb+K+
Li+Na+
329 nm
543 nm
339 nm
442 nm
Bi3+
6s
6s

Fig.8

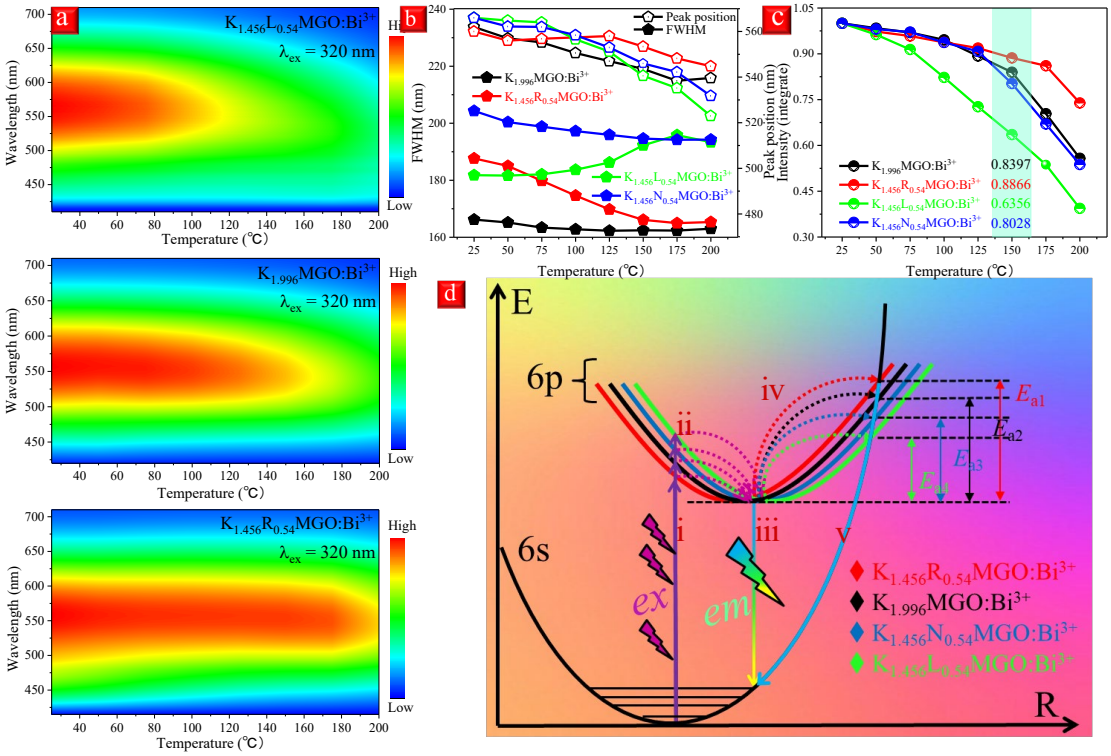
a
$K_{1.456}L_{0.54}MGO:Bi^{3+}$
λ_{ex} = 320 nm
Wavelength (nm)
Temperature (℃)
High
Low
$K_{1.996}MGO:Bi^{3+}$
λ_{ex} = 320 nm
$K_{1.456}R_{0.54}MGO:Bi^{3+}$
λ_{ex} = 320 nm
b
Peak position
FWHM
$K_{1.996}MGO:Bi^{3+}$
$K_{1.456}R_{0.54}MGO:Bi^{3+}$
$K_{1.456}L_{0.54}MGO:Bi^{3+}$
$K_{1.456}N_{0.54}MGO:Bi^{3+}$
FWHM (nm)
Peak position (nm)
c
Intensity (integrate)
$K_{1.996}MGO:Bi^{3+}$ 0.8397
$K_{1.456}R_{0.54}MGO:Bi^{3+}$ 0.8866
$K_{1.456}L_{0.54}MGO:Bi^{3+}$ 0.6356
$K_{1.456}N_{0.54}MGO:Bi^{3+}$ 0.8028
d
E
6p
6s
R
i
ii
iii
iv
v
ex
em
E_{a1}
E_{a2}
E_{a3}
E_{a4}
$K_{1.456}R_{0.54}MGO:Bi^{3+}$
$K_{1.996}MGO:Bi^{3+}$
$K_{1.456}N_{0.54}MGO:Bi^{3+}$
$K_{1.456}L_{0.54}MGO:Bi^{3+}$

Fig.9

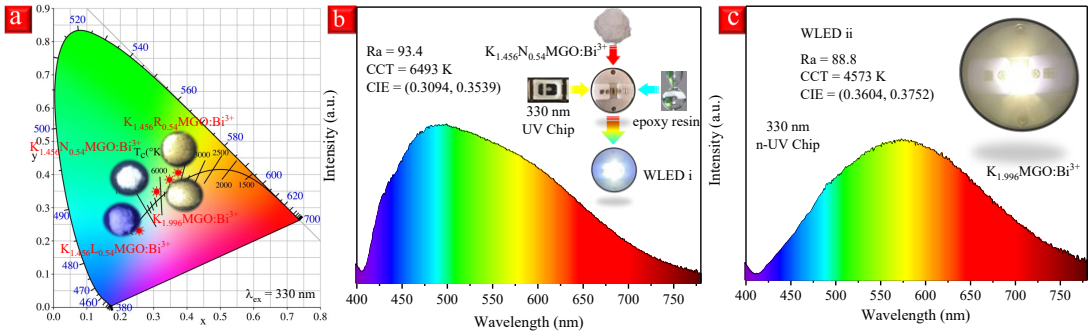
a
b
c
Ra = 93.4
CCT = 6493 K
CIE = (0.3094, 0.3539)
330 nm
UV Chip
epoxy resin
WLED i
Intensity (a.u.)
Wavelength (nm)
WLED ii
Ra = 88.8
CCT = 4573 K
CIE = (0.3604, 0.3752)
330 nm
n-UV Chip
λex = 330 nm